Optical Fiber Technology 80 (2023) 103452

Contents lists available at ScienceDirect

Optical Fiber Technology

journal homepage: www.elsevier.com/locate/yofte

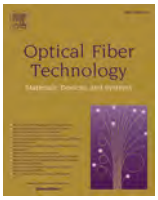

Low-temperature cross-sensitivity strain sensor based on a microbubble Fabry-Pérot interferometer with a thin wall

Jingwei Lv [a], Wei Li [a], Tongyu Meng [b], Qiao Li [a], Jianxin Wang [a], Xinchen Xu [a], Debao Wang [a], Wei Liu [a], Chao Liu [a,*], Paul K Chu [c]

[a] School of Physics and Electronic Engineering, Northeast Petroleum University, Daqing 163318, China
[b] Leicester International Institute, Dalian University of Technology, Dalian 124221, China
[c] Department of Physics, Department of Materials Science and Engineering, and Department of Biomedical Engineering, City University of Hong Kong, Tat Chee Avenue, Kowloon, Hong Kong, China

ARTICLE INFO

Keywords:
Fabry–Pérot interferometer
Air bubble
Optical fiber sensor
Strain sensitivity
Temperature cross-sensitivity

ABSTRACT

A Fabry-Pérot interferometer (FPI) strain sensor with low-temperature cross-sensitivity is prepared by a simple, cost-effective, and safe process. The sensor is fabricated by splicing two segments of the single-mode fiber and several arc discharges to form a unique circular bubble and a thin wall. The thin air-bubble wall deforms more easily under stress due to the good stress concentration ability of the tapered structure, resulting in a high strain sensitivity of 10.78 pm/με. The temperature sensitivity of the sensor is 1.24 pm/°C and the temperature cross-sensitivity is 0.115 με/°C in the temperature range of 25 to 200 °C, which reduces the temperature-induced measurement error. The experimental results show that the sensor with good stability and repeatability has large commercial potential in measuring strain in complex environments.

1. Introduction

Fiber optic sensors boasting low power loss, small size, low susceptibility to electromagnetic interference, and easy remote control are gradually replacing traditional electrical sensors in many sensing applications for temperature, refractive index, and strain [1–8]. Fiber optic sensors based on different principles have been demonstrated and studied, for instance, fiber Bragg gratings (FBGs) [9–11], Sagnac interferometers [12,13], Mach-Zander interferometers (MZIs) [14–16], and Fabry-Pérot interferometers (FPIs) [17–24]. Sensors based on FBG or MZI usually have a large temperature cross-sensitivity, and the temperature effects caused by thermo-optical or thermal expansion may produce extra spectral drifts. Therefore, temperature compensation is often required for accurate strain measurement consequently increasing the complexity of the sensing systems [25–28].

In strain measurements, FPI-based fiber optic sensors have the advantages of high sensitivity, linear response, low-temperature cross-sensitivity, and miniature size compared to other sensor structures [29,30]. Many methods have been proposed and demonstrated to fabricate microbubble FPI strain sensors. For example, Wu et al., have used a fusion splicer (FSM-45PM) to prepare FPI strain sensors for splicing single-mode fibers (SMF) and hollow-core fibers (HCF) with strain sensitivity and temperature cross-sensitivity of 3.29 pm/με and 0.328 με/°C, respectively, and have investigated the lateral loads and strain [17]. Cai et al., have proposed an asymmetrical micro air bubble FPI strain sensor. The micro air bubbles are formed by chemically etching an erbium-doped fiber (EDF) to attain a strain sensitivity of 10.15 pm/με and temperature cross-sensitivity of 0.42 με/°C [18]. However, the manufacturing process of these sensors involves complex pretreatment and hazardous chemicals, thus increasing the cost and production difficulty and the yield decreases due to the complex process. Even though the optimized fabrication process can be used to produce strain sensors with interference contrast up to 25 dB, it still remains challenging to further improve the temperature cross-sensitivity.

In this study, a Fabry-Pérot interferometer (ACFPI) with an approximately circular bubble and low temperature-strain sensitivity is designed and demonstrated. Two SMFs are fused to form the tiny bubble and different stresses are applied and released to produce an approximately circular bubble with an average wall thickness of 1.73 μm and diameter of 68 μm. The tapered structure and thin wall allow greater deformation under tensile stress resulting in an excellent strain sensitivity of 10.78 pm/με. In the temperature range of 25 – 200 ℃, the

* Corresponding author at: School of Physics and Electronic Engineering, Northeast Petroleum University, Daqing 163318, China.
E-mail address: msm-liu@126.com (C. Liu).

https://doi.org/10.1016/j.yofte.2023.103452
Received 27 May 2023; Received in revised form 20 July 2023; Accepted 20 July 2023
Available online 28 July 2023
1068-5200/© 2023 Elsevier Inc. All rights reserved.

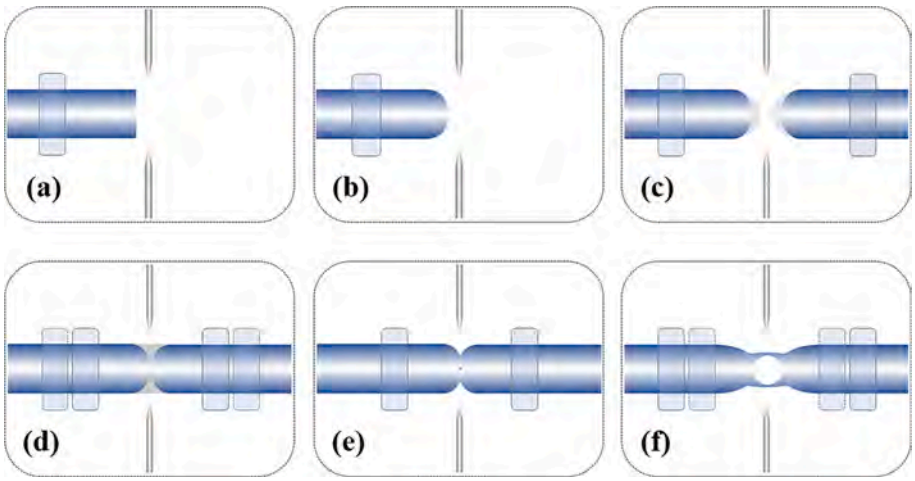

Fig.1. Schematics showing the fabrication of the ACFPI.

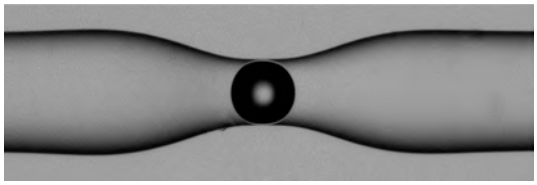

Fig. 2. Microscopic picture of the ACFPI.

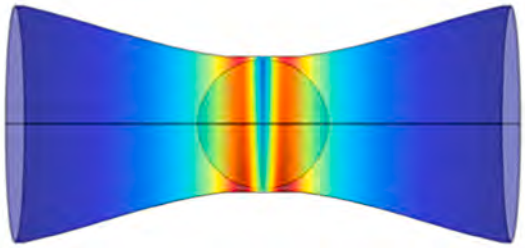

Fig. 3. Numerical simulation of the applied strain range of ACFPI.

temperature sensitivity of the sensor is 1.24 pm/℃ and the temperature cross-sensitivity is only 0.115 $\mu\varepsilon$/℃ consequently enabling precise strain measurements and a wide range of applications in civil structures, machinery and equipment, space shuttles and robotics.

2. Sensor fabrication and working principles

The manufacturing process of the sensor is safe, simple, and efficient, as shown in Fig. 1. Prior to the preparation, it was necessary to perform certain procedures. Specifically, the coating layer of the single mode fiber (SMF) was peeled off using a fiber Miller pliers and wiped with alcohol, and the SMF was cut smoothly with a fiber cutter, as shown in Fig. 1(a). The fiber was placed in a fiber fusion splicer (Fujikura 80 s) and adjusted to the proper position by the motor. Using the appropriate discharge time and discharge power, multiple discharges were produced to make the flat fiber end round and smooth, as shown in Fig. 1(b). The other SMF was prepared by a similar method, with both fibers dipped in a small amount of refractive-index-matching solution (Nd:1.47), so that the tips of both fibers were covered by the liquid. The refractive index matching solution is an oil-based material with the advantages of non-volatility and excellent adhesion, making it more suitable for experimental operations. The fibers were then placed in the fiber fusion splicer with both ends of the fibers to be fused fixed by the fiber presser feet, as shown in Fig. 1(c). By manipulating the left and right motors, as shown in Fig. 1(d), the end surfaces of the curved fibers were surrounded by the liquid and a slight displacement was applied on top to squeeze the two SMFs. By adjusting the discharge time and discharge power of the 80 s fusion splicer, a micro air bubble was formed as shown in Fig. 1(e). The size of the fiber bubble was monitored during further discharging, and the pull pressure, discharge time, and discharge power were adjusted continuously to obtain the microbubble as shown in Fig. 1(f).

The fiber-optic microbubble composed of all-quartz materials with the circular shape is located in the middle of the fiber and Fig. 2 depicts the microscopic image. The discharge power and discharge time determine the rate of air bubble formation and the final air bubble wall thickness. By precisely controlling the discharge power, the wall

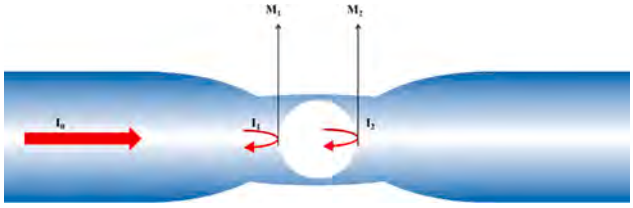

Fig. 4. Schematic diagram showing the air bubble in the ACFPI.

thickness can be reduced to approximately 1.73 μm. The wall thickness and applied tensile stress determine the radius of the bubble and precise control of the tensile stress leads to the sensor microbubble length of only 68 μm. The small bubble not only improves the strain sensitivity of the sensor, but also is promising in microstrain monitoring and integration.

When the external environment changes, the sensor undergoes a small deformation and the cavity length changes accordingly, causing the reflection spectrum of light in the bubble to drift, using this method to achieve the sensing function of ACFPI。 Except for FPI, there are also fiber Bragg grating sensors, which have a strain sensitivity of only 2 pm/με [21], but it requires the requires the discrimination of thermal strain and pure force-induced strain of the sensing point in high-temperature strain measurement [31]. The bubble structure of the Fabry-Pérot sensor has a thinner wall thickness, which allows the strain to act better on the FP cavity as shown in Fig. 3, thus having a greater effect on the variation of the cavity length and therefore a higher strain sensitivity.

The schematic and working principle of the fiber optic sensor are ilustrated in Fig. 4, in which M_1 and M_2 are the two reflective surfaces of the air cavity and the light intensity from the continuous light source into the fiber is I_0. Light reaching the M_1 reflective surface undergoes first reflection. The reflected light intensity is I_1 and part of the light

passes through the air cavity to M_2 to undergo second reflection. The reflected light intensity is I_2, and the two beams of reflected light coupled in the single-mode fiber core produce interference.

Given that the reflection energy of quartz/air is only 4%, it can be observed that the third reflected light intensity inside the bubble is a mere 0.006% when the bubble allows for the complete trasmission of the light intensity, the higher-order reflected light energy is very weak and almost negligible, so we consider it as double-beam interference, namely Fabry-Pérot interference. With regard to two-beam interference, the interference spectrum can be expressed as:

$$I = I_1 + I_2 + 2\sqrt{I_1 I_2}\cos(\theta) \tag{1}$$

where θ is the phase difference shift caused by transmission of light in the air cavity. The reflection spectrum exhibits the cosine characterstics in two-beam interference. The Free Spectral Range (FSR) of interfering spectrum can be given by Eq. (1) as:

$$FSR = \lambda_{m+1} - \lambda_m \text{ , and} \tag{2}$$

$$FSR = \frac{\lambda_{m+1}\lambda_m}{2n_{eff}L} \tag{3}$$

where m is the number of fiber interference levels and λ_m is the FPI resonant wavelength position corresponding to the interference level, n_{eff} is the refractive index of air, and L is the length of the air bubble.

The change in FPI cavity length can be derived by calculating the change in the position of the peak spectral resonance:

$$\delta L/L \approx \delta\lambda/\lambda \tag{4}$$

where δL is the amount of cavity length variation and $\delta\lambda$ is the change of wavelength. In summary, the cavity length L variation can be calculated or monitored in real time based on the interference spectral FSR.

Strain is a physical quantity that measures the magnitude of deformation of an object, and measuring deformation using the FPI method is the most direct and effective way. A change in the strain magnitude alters the cavity length and causes a drift in the fiber FPI spectrum as shown in the following:

$$\Delta\lambda = k_{FP}\varepsilon_{FP} \tag{5}$$

where k_{FP} is the strain coefficient of the FP cavity and ε_{FP} is the magnitude of the applied strain on the fiber. The cavity length of the bubble cavity is too small compared to the fiber length and is negligible. Hence, the change in the cavity length is determined by the volume change of the FPI and the cross-sectional area is given by:

$$\Delta\varepsilon_{FP}E\pi\left(d_{fiber}^2 - d_{FP}^2\right) = \Delta\varepsilon_{fiber}E\pi d_{fiber}^2 \tag{6}$$

where E is the Young's modulus of the fiber and d is the radius of the section corresponding to the subscript.

The strain exerted by the microbubble in the fiber is [32]:

$$\varepsilon_{FP} = \frac{\Delta L_{FP}}{L_{FP}} \tag{7}$$

Combining the above equations, the strain relationship between the fiber optic sensor and bubble cavity is obtained as follows:

$$\varepsilon = \frac{L_{FP} + L_{fiber}\frac{d_{fiber}^2 - d_{FP}^2}{d_{fiber}^2}}{L_{FP} + L_{fiber}}\varepsilon_{FP} \tag{8}$$

Combining Eq. (3) and Eq. (7), the strain sensitivity of the sensor is obtained as follows:

$$k = \frac{\Delta\lambda}{\varepsilon} = k_{FP}\frac{L_{FP} + L_{fiber}}{L_{FP} + L_{fiber}\frac{d_{fiber}^2 - d_{FP}^2}{d_{fiber}^2}} \tag{9}$$

In this sensor, the wall thickness is reduced to increase the bubble radius, and it can be seen from Eq. (8) that the bubble radius is proportional to the strain sensitivity of the sensor and the strain sensitivity increases with the increase of the radius.

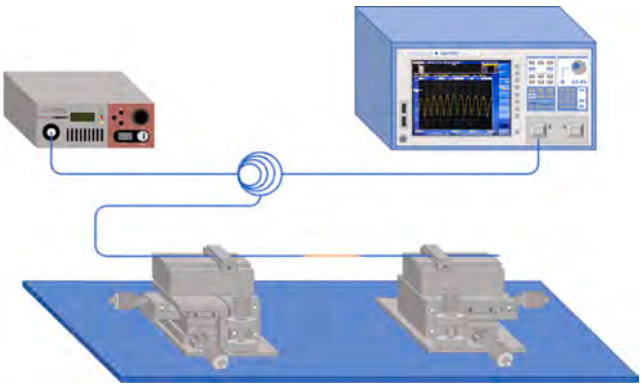

Fig.5. Optical fiber strain platform.

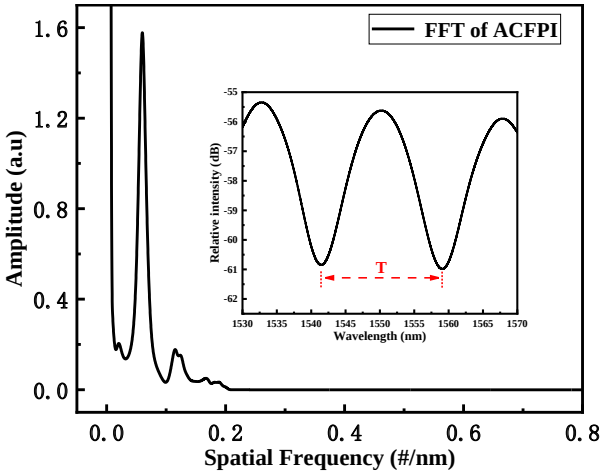

Fig. 6. Spatial frequency spectra of ACFPI.

When the environmental temperature changes, the mode index difference Δn and SMF length L_{SMF} also change accordingly, and the reflection spectrum has a wavelength shift Δλ. The temperature response of the interferometer is

$$\frac{\Delta\lambda}{\lambda} \approx (\alpha + \xi)\Delta T \tag{10}$$

where $\Delta\lambda/\lambda$ is the relative wavelength shift caused by temperature change ΔT, α and ξ are the thermal expansion coefficient and thermo-optical coefficient of the SMF material, respectively. It can be found that the wavelength shift caused by the temperature change is only determined by the properties of the SMF material.

3. Results and discussion

An appatus depicted in Fig. 5 is set up to investigate the strain characteristics of ACFPI. A 3 dB ring coupler is connected to the SuperK COMPACT (SC, 450–2500 nm) on one end and to the optical spectrum analyzer (OSA, resolution 0.02 nm) on the other end. The fiber optic sensor is placed in the middle of two three-dimensional (3D) moving stages and axial stress is applied to the sensor by rotating the knob. For linear deformation, the strain is defined as the ratio of the change to the initial amount as shown in Eq. (7). Since the sensor has a limited strain tolerance, it is imperative to avoid selecting a small distance L of the three-dimensional moving platform during the experiment, because the

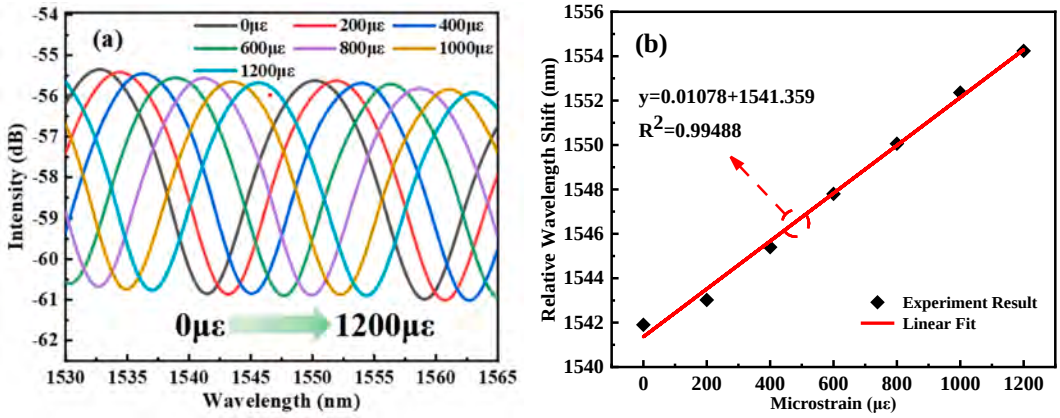

Fig. 7. Strain response of the ACFPI: (a) Reflection spectra of the ACFPI for different strain levels and (b) Relationship between the strain and wavelength drift of the ACFPI.

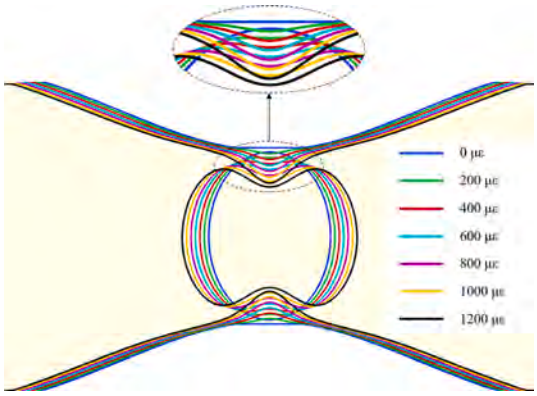

Fig. 8. Deformation of the sensor under 0–1200 με tensile stress.

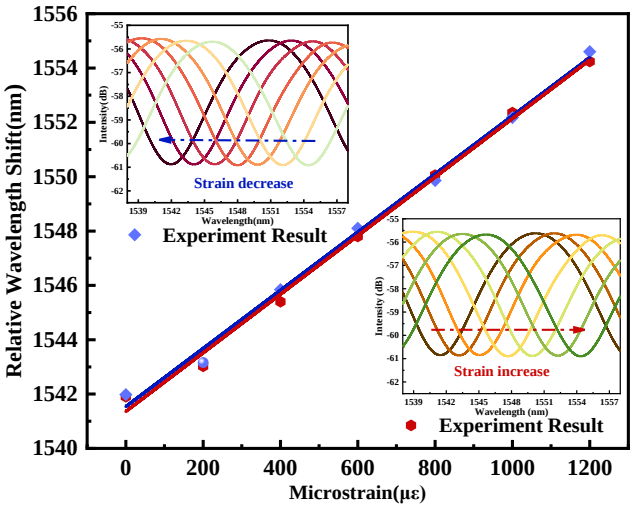

Fig. 9. Reproducibility of the results of the ACFPI.

sensor can be easily damaged if the distance is too small. Therefore, by fixing the distance between the two moving platforms at 10 cm, the sensor is subjected to 100 με for each 10 μm step and the amount of axial stress applied to the sensor is changed.

Fast Fourier transform is performed on the reflection spectra of the ACFPI structure as shown in Fig. 6. There is only one strong peak proving two-beam interference. In other words, the structure has an all single-component Fabry-Pérot cavity. As shown in Fig. 6, the reflection spectrum exhibits the required cosine characteristics for two-beam interference.

The deformation of a microbubble in the fiber optic strain sensor under external stress produces a drift in the interference peak, which can be utilized to determine the magnitude of the stress. Fig. 7(a) shows the different stress profiles ranging from 0 με to 1200 με at room temperature. The microbubble fiber is fixed on a three-dimensional moving platform, and the length of the microbubbles in the fiber is changed during the application of 0–1200 με, which results in a red-shift of the sensor's interference spectrum, as well as a total wavelength drift of about 15 nm. Because of the unique circular structure, Fig. 7(a) shows $\lambda_m = 1541.46$ nm and $\lambda_{m+1} = 1559.08$ nm at a wavelength of 1,550 nm. The FSR is 17.62 nm according to Eq. (2) and the bubble length is 68.197 μm according to Eq. (3). The microscopic image reveals that the actual bubble length is 68 μm, indicative of an error of only 0.197%. The linear relationship between stress and wavelength drift at different strain levels in Fig. 7(b) shows an R^2 of 0.99488 indicating good linearity. Based on the fitted wavelength drift to stress, the slope shows that the strain sensitivity is 10.78 pm/με.

Numerical simulations are conduted on the ACFPI to explore the underlying mechanism of the high strain sensitivity. Fig. 8 illustrates the deformation of the microbubble inside the embedded sensor with 20-fold magnification, corresponding to the increase of the axial length from 0 to 1200 με in steps of 200 με. Eq. (4) provides that the horizontal length of the bubbles increases by 0.47 μm and the vertical length of the bubbles decreases by 0.433 μm. The tensile stress is concentrated in the thinnest part of the bubble wall, accompanied by a slight depression and significant bubble deformation. Subsequently, the length of the bubble is amplified, indicating enhanced extensibility and greater detection capacity.

Fig. 9 shows the linearly fitted curves of the forward applied stress and reverse released stress. The strain sensitivity is obtained by two groups of experiments on the fiber with forward applied stress and reverse released stress. The repeatability is verified by comparing the stability of the sensitivity in the two stages. In the forward applied stress phase, the axial stress on the sensor increases from 0 με to 1200 με, and the strain sensitivity of the sensor is 10.78 pm/με. In the opposite stress release phase, the axial stress decreases from 1200 με to 0 με, and the strain sensitivity of the sensor is 10.7 pm/με, with a wavelength drift recorded every 200 με. The two curves exhibit a high degree of overlap demonstrating consistent strain sensitivity and good repeatability.

The stability test of the ACFPI is conducted at room temperature with the stress applied to the sensor in the forward direction ranging from 0 με to 1,200 με. Each change in a stress of 200 με is recorded after holding for 5 min. The stability of the sensor is demonstrated by the consistency of the trough of the reflection spectrum at around 1,550 nm

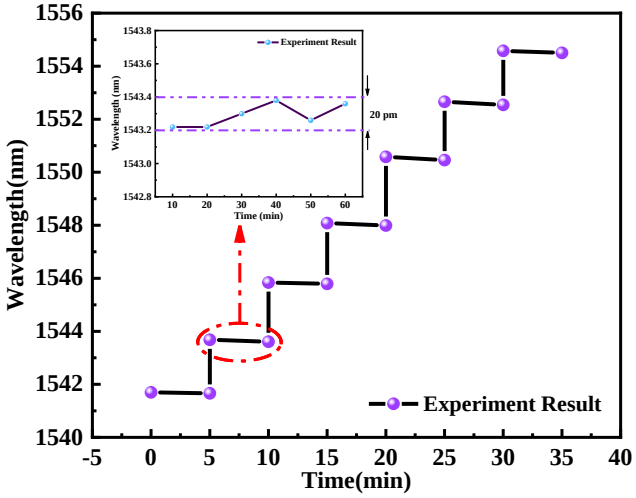

Fig. 10. Stability of the sensor.

at different axial strains, as illustrated in Fig. 10. In order to conduct a more comprehensive analysis on the stability of the ACFPI, the axial strain is kept at 200 με to obtain the wavelength shift in 60 min. Fig. 10 shows that the sensor has favorable stability, as the interference fringe variation remains below 20 pm.

The refractive index of the optical fiber and length of the bubble changes in response to changes in the external environment, which affect the phase of the sensor. This alteration generates an optical range difference, which subsequently causes a shift in the interference peak of the FPI sensor's interference spectrum. To prevent any displacement of the fiber during the temperature experiment, the fiber optic sensing section is secured on a metal base. The temperature is ramped up from 25 °C to 200 °C in steps of 25 °C using a constant temperature platform, and the interference spectra are acquired at each temperature, as shown in Fig. 11(a). The reflection spectra do not drift significantly with temperature, proving that the sensor does not experience thermal expansion. As shown in Fig. 11(b), the relationship between the wavelength drift and temperature is derived by linear fitting of the trough at 1,541 nm. The temperature sensitivity of the ACFPI is found to be 1.24 pm/°C and the temperature cross-sensitivity is 0.115 με/°C, indicating a relatively low sensitivity to temperature.

In order to do a comprehensive evaluation, we compare the performance parameters of our device with those of previously reported works. These parameters include the strain range, temperature sensitivity, strain sensitivity, and temperature cross-sensitivity. As shown in Table 1, our sensor exhibits lower temperature cross-sensitivity than the other sensors [17–24]. The unique circular ACFPI with a thin wall thickness highly reflective surface provides significant structural advantageous and these features renders the fiber insensitive to temperature. More importantly, the sensor is easy to produce without needing expensive equipment and hazardous chemicals making the manufacturing process safer and more economical.

4. Conclusion

An ACFPI with a low temperature-strain sensitivity is designed and demonstrated. A spectrometer is used to analyze the interferometric spectrum of the ACFPI to obtain the sensitivity parameters of the fiber. Experimental results show that the strain sensitivity is as high as 10.78 pm/με in the range of 0 to 1,200 με, and the temperature sensitivity is 1.24 pm/°C from 25 to 200 °C. These favorable characteristics stem from precise control of the parameters and a structure with a distinctive air bubble. This structure not only has a thin bubble wall, but also allows a large measurement range without affecting the strain sensitivity. The temperature cross-sensitivity of the sensor is only 0.115 με/°C,

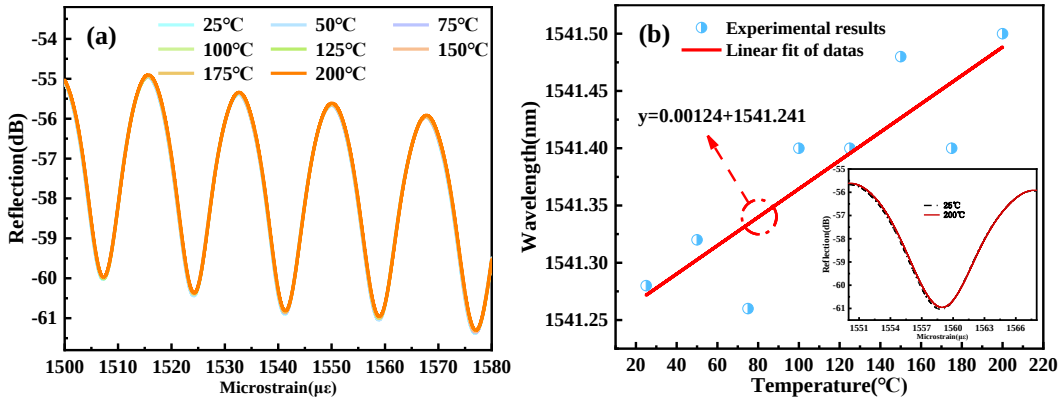

Fig. 11. Temperature Response of the ACFPI: (a) Reflection spectra of the sensor at different temperature and (b) Relationship between the dip wavelength shift and temperature.

Table 1
Comparison of our and previously reported sensors.

Types	Strain range (με)	Temperature sensitivity (pm/℃)	Strain sensitivity (pm/με)	Temperature cross-sensitivity (με/°C)	References
Special air cavity FPI	0–1100 με	1.08 pm/℃	3.29 pm/με	0.328 με/°C	[17]
Unsymmetrical air-microbubble FPI	0–1200 με	2.4 pm/℃	10.15 pm/με	0.42 με/°C	[18]
FPI based on an alumina ceramic derived fiber	0–3000 με	15.61 pm/℃	1.5 pm/με	10.41 με/°C	[19]
Rounded rectangular Air-cavity FPI	0–1200 με	1.79 pm/℃	8 pm/με	0.224 με/°C	[20]
SMF-FMF-FBG	0–450 με	34.3 pm/℃	2 pm/με	17.15 με/°C	[21]
A high sensitivity stain sensor based on MZI	0–2100 με	1.6 pm/℃	2.7 pm/με	0.593 με/°C	[22]
Ultra-Sensitive Strain Sensor Based on Femtosecond Laser	0–1600 με	~278.48 pm/℃	~28.11 pm/με	~9.91με/°C	[23]
Sapphire derived fiber based FPI	0–1000 με	15.41 pm/℃	1.25 pm/με	12.328 με/°C	[24]
An approximately circular microbubble FPI	0–1200 με	1.24 pm/℃	10.78 pm/με	0.115 με/°C	This work

indicating high temperature tolerance and small relative temperature errors. In addition to the high strain sensitivity, low temperature sensitivity, as well as good repeatability and stability, the manufacturing process is simple, cost-effective, and safe. Therefore, the sensor has great potential in applications such as micro-strain monitoring.

CRediT authorship contribution statement

Jingwei Lv: Conceptualization, Data curation, Writing – review & editing. **Wei Li:** Conceptualization, Methodology, Software, Writing – original draft. **Tongyu Meng:** Methodology, Supervision. **Qiao Li:** Investigation. **Jianxin Wang:** Formal analysis. **Xinchen Xu:** Funding acquisition, Validation. **Debao Wang:** Formal analysis. **Wei Liu:** Software, Validation. **Chao Liu:** Validation. **Paul K Chu:** Project administration.

Declaration of Competing Interest

The authors declare that they have no known competing financial interests or personal relationships that could have appeared to influence the work reported in this paper.

Data availability

No data was used for the research described in the article.

Acknowledgments

This work was jointly supported by the Outstanding Young and Middle-Aged Research and Innovation Team of Northeast Petroleum University [KYCXTD201801], Local Universities Reformation and Development Personnel Training Supporting Project from Central Authorities, Natural Science Foundation of Heilongjiang Province [grant number LH2021F007], China Postdoctoral Science Foundation funded project [grant number 2020M670881], City University of Hong Kong Strategic Research Grant (SRG) [grant number 7005505], and City University of Hong Kong Donation Research Grant [grant number DONRMG No. 9229021]. Study Abroad returnees merit based Aid Foundation in Heilongjiang Province (070-719900103), Northeastern Petroleum University scientific research projects (2019KQ74).

References

[1] C. Liu, J. Lü, W. Liu, F. Wang, P.K. Chu, Overview of refractive index sensors comprising photonic crystal fibers based on the surface plasmon resonance effect [Invited], Chin. Opt. Lett. 19 (2021), 102202.
[2] W. Liu, Y. Shi, Z. Yi, C. Liu, F. Wang, X. Li, J. Lv, L. Yang, P.K. Chu, Surface plasmon resonance chemical sensor composed of a microstructured optical fiber for the detection of an ultra-wide refractive index range and gas-liquid pollutants, Opt. Express 29 (2021) 40734–40747.
[3] W. Liu, C. Liu, J. Wang, J. Lv, Y. Lv, L. Yang, N. An, Z. Yi, Q. Liu, C. Hu, P.K. Chu, Surface plasmon resonance sensor composed of microstructured optical fibers for monitoring of external and internal environments in biological and environmental sensing, Results Phys. 47 (2023), 106365.
[4] Y. Zeng, J. Lv, H. Fu, X. Wu, L. Yang, W. Liu, Z. Yi, Q. Liu, C. Hu, Y. Lv, P.K. Chu, C. Liu, HE1,1 mode excited surface plasmon resonance for high-sensitivity sensing by photonic crystal fibers, J. Opt. Soc. Am. A 40 (2023) 35–44.
[5] W. Liu, C. Hu, L. Zhou, Z. Yi, C. Liu, J. Lv, L. Yang, P.K. Chu, A square-lattice D-shaped photonic crystal fiber sensor based on SPR to detect analytes with large refractive indexes, Physica E 138 (2022) 115106.
[6] X. Luhui, L. Chao, F. Haihao, W. Jianxin, L. Xianli, L. Jingwei, Y. Lin, K.C. Paul, Orbital angular momentum-excited surface plasmon resonance for liquid refractive index sensing by photonic crystal fiber with high sensitivity and wide detection range, Opt. Eng. 61 (2022), 096101.
[7] K. Bohnert, P. Gabus, J. Kostovic, H. Brändle, Optical fiber sensors for the electric power industry, Opt. Lasers Eng. 43 (2005) 511–526.
[8] L. Palmieri, D. Sarchi, A. Galtarossa, Distributed measurement of high electric current by means of polarimetric optical fiber sensor, Opt. Express 23 (2015) 11073–11079.
[9] C. Campanella, A. Cuccovillo, C. Campanella, A. Yurt, V. Passaro, Fibre bragg grating based strain sensors review of technology and applications, Sensors 18 (9) (2018) 3115.
[10] S. Sulejmani, C. Sonnenfeld, T. Geernaert, G. Luyckx, D. Van Hemelrijck, P. Mergo, W. Urbanczyk, K. Chah, C. Caucheteur, P. Mégret, H. Thienpont, F. Berghmans, Shear stress sensing with Bragg grating-based sensors in microstructured optical fibers, Opt. Express 21 (2013) 20404–20416.
[11] P. Ferraro, G. De Natale, On the possible use of optical fiber Bragg gratings as strain sensors for geodynamical monitoring, Opt. Lasers Eng. 37 (2-3) (2002) 115–130.
[12] J. Sadeghi, H. Latifi, M. Murawski, F. Mirkhosravi, T. Nasilowski, P. Mergo, K. Poturaj, Group polarimetric pressure sensitivity of an elliptical-core side-hole fiber at telecommunication wavelengths, IEEE J. Sel. Top. Quantum Electron. 22 (2) (2016) 49–54.
[13] Q. Liu, L. Xing, Z. Wu, L.u. Cai, Z. Zhang, J. Zhao, High-sensitivity photonic crystal fiber force sensor based on Sagnac interferometer for weighing, Opt. Laser Technol. 123 (2020) 105939.
[14] X. Dong, H. Du, X. Sun, Z. Luo, Ji'an Duan, A Novel strain sensor with large measurement range based on all fiber Mach-Zehnder interferometer, Sensors 18 (5) (2018) 1549.
[15] L.M. Hu, C.C. Chan, X.Y. Dong, Y.P. Wang, P. Zu, W.C. Wong, W.W. Qian, T. Li, Photonic crystal fiber strain sensor based on modified mach-zehnder interferometer, IEEE Photonics J. 4 (1) (2012) 114–118.
[16] C.R. Liao, D.N. Wang, Y. Wang, Microfiber in-line Mach-Zehnder interferometer for strain sensing, Opt. Lett. 38 (2013) 757–759.
[17] Y. Wu, Y. Zhang, J. Wu, P. Yuan, Temperature-insensitive fiber optic Fabry-Perot interferometer based on special air cavity for transverse load and strain measurements, Opt. Express 25 (2017) 9443–9448.
[18] L. Cai, J. Wang, M. Chen, X. Ai, A high-sensitivity strain sensor based on an Unsymmetrical air-microbubble Fabry-Pérot interferometer with an ultrathin wall, Measurement 181 (2021), 109651.
[19] Z. Wang, H. Liu, Z. Ma, Z. Chen, T. Wang, F. Pang, High temperature strain sensing with alumina ceramic derived fiber based Fabry-Perot interferometer, Opt. Express 27 (2019) 27691–27701.
[20] Q. Li, J. Wang, H. Mu, J. Lv, L. Yang, Y. Shi, Z. Yi, P.K. Chu, Q. Liu, C. Liu, A Fabry-Pérot interferometer strain sensor composed of a rounded rectangular air cavity with a thin wall for high sensitivity and interference contrast, Opt. Commun. 527 (2023), 128920.
[21] X. Gao, T. Ning, C. Zhang, J. Xu, J. Zheng, H. Lin, J. Li, L. Pei, H. You, A dual-parameter fiber sensor based on few-mode fiber and fiber Bragg grating for strain and temperature sensing, Opt. Commun. 454 (2020), 124441.
[22] L. Dong, T. Gang, C. Bian, R. Tong, J. Wang, M. Hu, A high sensitivity optical fiber strain sensor based on hollow core tapering, Opt. Fiber Technol. 56 (2020), 102179.
[23] J. Deng, D.N. Wang, Ultra-sensitive strain sensor based on femtosecond laser inscribed in-fiber reflection mirrors and vernier effect, J. Lightwave Technol. 37 (2019) 4935–4939.
[24] P. Zhang, L. Zhang, Z. Wang, X. Zhang, Z. Shang, Sapphire derived fiber based Fabry-Perot interferometer with an etched micro air cavity for strain measurement at high temperatures, Opt. Express 27 (2019) 27112–27123.
[25] A.D. Kersey, M.A. Davis, H.J. Patrick, M. LeBlanc, K.P. Koo, C.G. Askins, M. A. Putnam, E.J. Friebele, Fiber grating sensors, J. Lightwave Technol. 15 (1997) 1442–1463.
[26] J.Z. Li, Y.L. Du, C.X. Liu, Attached FBG strain sensor based on thermal stress mechanism, Adv. Mat. Res. 216 (2011) 91–95.
[27] M. Sun, B. Xu, X. Dong, Y. Li, Optical fiber strain and temperature sensor based on an in-line Mach-Zehnder interferometer using thin-core fiber, Opt. Commun. 285 (2012) 3721–3725.
[28] B. Xu, M. Chen, K. Yang, Y. Guo, D.N. Wang, C.-L. Zhao, Ultra-high sensitivity strain sensor based on biconical fiber with a bulge air-bubble, Opt. Lett. 46 (2021) 1983–1986.
[29] M. Shao, Z. Cao, H. Gao, M. Hao, X. Qiao, Large measurement-range and low temperature cross-sensitivity optical fiber curvature sensor based on Michelson interferometer, Opt. Fiber Technol. 72 (2022), 102990.
[30] Z. Lu, C. Liu, C. Li, J. Ren, L. Yang, Ultra-High Sensitivity and Temperature-Insensitive Optical Fiber Strain Sensor Based on Dual Air Cavities, Materials2023.
[31] P. Xia, Y. Tan, C. Yang, Z. Zhou, K. Yun, A composite fabry-perot interferometric sensor with the dual-cavity structure for simultaneous measurement of high temperature and strain, Sensors 21 (15) (2021) 4989.
[32] Y.-J. Rao, M. Deng, D.-W. Duan, X.-C. Yang, T. Zhu, G.-H. Cheng, Micro Fabry-Perot interferometers in silica fibers machined by femtosecond laser, Opt. Express 15 (2007) 14123–14128.